Disruption of Plasma Membrane Lipid Asymmetry Alters Cellular Energetics

Authors: Pavel Barahtjan[1,2], Katelyn C. Cook[1], Václav Bočan[1], H. Mathilda Lennartz[1], Tobias Jumel[1], Kai Schuhmann[1], Sofia Traikov[3], Kristin Böhlig[1], Sascha M. Kuhn[1], Cristina Jiménez López[1], Tiago C. Alves[3,4], Andrej Shevchenko[1], Jonathan Rodenfels[1,5]* & André Nadler[1]*

Affiliations:
[1]Max-Planck-Institute of Molecular Cell Biology and Genetics, Dresden, 01307, Germany
[2]Interfaculty Institute of Bioengineering and Global Health Institute, École Polytechnique Fédérale de Lausanne (EPFL), Lausanne, 1015, Switzerland
[3]Institute for Clinical Chemistry and Laboratory Medicine, Universitätsklinikum Carl Gustav Carus, Technical University Dresden, Germany
[4]DZD-Paul Langerhans Institute of the Helmholtz Zentrum München, Germany
[5]Cluster of Excellence Physics of Life, Technical University Dresden, Dresden, Germany

*Corresponding authors. Email: rodenfels@mpi-cbg.de & nadler@mpi-cbg.de

Abstract: Biological membranes often feature an unequal and actively maintained concentration gradients of lipids between bilayer leaflets, termed lipid asymmetry.[1–3] Lipid asymmetry has been linked to many cellular processes[4,5], but the mechanisms that connect lipid trans-bilayer concentration gradients to cellular functions are poorly understood. Here we systematically map the cellular processes affected by dysregulation of lipid asymmetry by knocking out flippases, floppases, and scramblases in mammalian cells. We identify broad alterations to core metabolic pathways including nutrient uptake, neutral lipid turnover, pentose phosphate pathway and glycolysis. Lipidomics, respirometry, lipid and metabolic imaging, and live-cell calorimetry revealed elevated neutral lipid and ATP consumption rates which are coupled with increased heat loss per unit of biomass synthesized despite slower growth. This suggests that compensatory maintenance of lipid asymmetry strains the cellular energy budget, inducing a shift from a growth-promoting anabolic to a more energy-using catabolic state. Our data indicate that lipid asymmetry and its active maintenance is key for proper cell energetics, highlighting its putative role as a cellular store of potential energy akin to proton and ion transmembrane gradients.

Main Text

The plasma membranes of eukaryotes and bacteria display an asymmetric lipid distribution between the inner and outer bilayer leaflets, far removed from thermodynamic equilibrium [1–4,6–8]. Lipid asymmetry constitutes a trans-bilayer lipid concentration gradient. Maintaining the steady-state lipid concentration gradient requires actively driven lipid flows across the membrane, which are generated and controlled by lipid translocases. Specifically, flippases and floppases (P_4-ATPases and ABC transporters) move lipids against the gradient in an ATP-dependent, substrate-specific manner.[5,9,10] ATP-independent scramblases equilibrate lipid distribution between the bilayer leaflets (Fig. 1A).[5,11–13]

In mammals, lipid asymmetry has been linked to numerous cellular processes, including apoptosis[14,15], muscle development[16–19], fertilization[20–22], blood coagulation[23,24] and a number of immune signaling processes[25–30]. Furthermore, externalization of phosphatidylserine (PS) has been associated with neuronal functions[31], including synaptic pruning[32,33], axonal regeneration[34] , and photoreceptor function[35]. Certain mutations in genes encoding scramblases and flippases cause hereditary diseases, including bleeding disorders, hearing loss and an progressive familial intrahepatic cholestasis type 1[36–39]. While these findings highlight the importance of lipid asymmetry for eukaryotic physiology, the overarching mechanisms that link trans-bilayer lipid concentration gradients to cell biological function remain unknown: Why is lipid asymmetry is required for cell biological function in the first place?

Several hypotheses regarding the cellular functions of lipid asymmetry have been proposed.[3,4,40] In a biophysical interpretation, the highly ordered outer leaflet could serve as a protective barrier, whereas more fluid inner leaflet constitutes a platform for catalyzing biochemical reactions. Lipid asymmetry could also be involved in the regulation of lipid-protein interactions through sequestration of lipids on opposing membrane leaflets. Finally, lipid asymmetry could constitute a store of potential energy similar to ion or proton gradients across cellular membranes.[2,41] In this case, lipid flippases and floppases would be equivalent to ion pumps, whereas scramblases would act as ion channel analogues. While all of these hypotheses are intuitively appealing, very little evidence supports any of them.

To comprehensively understand the biology of lipid asymmetry, a systematic approach is required. We thus generated a series of CRISPR-mediated knockouts (KOs) of lipid flippases, floppases, and scramblases in the plasma membrane of mammalian cells. For each KO line, we performed a systems-level analysis of transcriptomic, proteomic, and lipidomic alterations, with large-scale dataset integration to identify shared cellular processes influenced by lipid asymmetry (Fig. 1B). We discovered a broad-spectrum regulation of cellular metabolic pathways extending from transmembrane solute transport to glycolysis, mitochondrial energy production, and biosynthesis of lipids, peptides, nucleic acids, and carbohydrates in addition to previously identified alterations to immune response, cell adhesion, and differentiation. We further validated the role of P_4-ATPase flippases in energy metabolism by a series of biochemical assays. We found lower steady-state levels and faster consumption of triacylglycerols (TAGs) and higher ATP consumption rates. Flippase KO lines displayed slower growth, increased mass-specific metabolic rates, and elevated heat loss per unit of synthesized biomass, implying a shift from anabolic biomass production to a more catabolic state. Altogether, we identify a direct link between lipid asymmetry and cellular metabolism and provide evidence in support of a fundamental function for lipid bilayer asymmetry in cellular energetics, which is expected if lipid concentration gradients serve as energy stores.

Results

Loss of lipid asymmetry mediators leads to altered lipid trans-bilayer movement.

We chose the HCT116 epithelial colon cancer cell line as our model system, as it harbors a near-diploid chromosome number and provides context for the gut-immune system, the gut-brain axis, and metabolism. As targets for genetic modification, we chose plasma membrane-resident lipid translocases and scramblases that we found to be expressed in HCT116 cells: ANO6 and PLSCR1 (scramblases); ABCA1 and ABCA7 (floppases); ATP8A1, ATP11A, ATP11C, ATP8B1, and ATP8B2 (flippases); and the shared flippase subunit TMEM30A (used in our previous study[42]). Most of these proteins are unambiguously confirmed as components of the lipid asymmetry machinery with strong structural and biochemical evidence.[11,38,43,44]

We employed CRISPR-mediated deletion of the critical exon present in all protein isoforms for each respective gene and confirmed knockout by measuring read coverage for RNA transcripts (Extended Data Fig. 1A). Full deletion of the target exons was achieved for all candidates except TMEM30A, which retained a small fraction of the target transcript. We further confirmed this at the protein level, finding that approximately 30% of TMEM30A abundance remained after knockout, whereas other lipid asymmetry proteins were un-detectable (Extended Data Fig. 1B).

Next, we assessed the impact of lipid asymmetry knockouts on cellular lipid levels using quantitative shotgun lipidomics. We monitored major classes of membrane lipids including glycerophospholipids (PS, PE, PC, PI, including ether lipids), sphingolipids (Cer, HexCer and SM), Cholesterol and neutral lipids (CE, DG and TAG). We found that PE levels were uniformly elevated, while the molar abundances of TAGs and PC ether lipids were decreased (Extended Data Fig. 2A,B). Most other lipid classes were unaffected (Extended Data Fig. 2A,B). Among the main lipid substrates of the lipid translocases in our study, only PE was increased across all KO lines. Among glycerophospholipids, species comprising short chain (14 to 15 carbon atoms and 0 to 1 double bonds per fatty acid moiety) were enriched regardless of the lipid class. This was particularly pronounced for P_4-ATPase KO lines (Fig. 1C). This trend was balanced by changes of longer-chain species resulting in an overall conservation of the average phospholipid chain-length (Extended Data Fig. 2D, 3). These compensatory changes were cell line-specific, potentially due to the need to maintain constant bilayer thicknesses. We hypothesized that these species level changes were due to the substrate-specificity of the lipid asymmetry machinery.

To test this hypothesis and to functionally validate the lipid asymmetry lines we measured PE internalization kinetics. Given their function as lipid translocases at the plasma membrane, we expected our KO lines to exhibit slower trans-bilayer movement and subsequent internalization of exogenously delivered lipids. We recently discovered that retrograde PE trafficking from the plasma membrane to internal membranes occurs predominantly via non-vesicular lipid transport [42], making PE internalization rates a valuable proxy for lipid flipping rates. We measured lipid internalization with near-native bifunctional lipid probes functionalized with diazirine and alkyne moieties, which can be photochemically cross-linked to cellular proteins and visualized by fluorescence microscopy (Extended Data Fig. 4A). Bifunctional lipids were incorporated into the outer leaflet of the plasma membrane and internalization monitored in pulse-chase experiments. We compared internalization kinetics for PE(18:1/Y_{16}) (with Y denoting a 16-carbon bifunctional fatty acid), which mimics the PE34:1 species that was not altered in our lipidomics data (Fig. 1C), and PE(14:0/Y_{14}) (with Y_{14} denoting a 14-carbon bifunctional fatty acid), which serves as a model for the medium-chain aminophospholipids which are upregulated in the flippase KOs. In wildtype (WT) cells,

PE(18:1/Y_{16}) was transported slightly faster than PE(14:0/Y_{14}) (Fig. 1D/E). In ATP8B1, ATP11C, and TMEM30A KOs, PE(14:0/Y_{14}) transport was largely unaffected. In contrast, the PE(18:1/Y_{16}) species was internalized slower, remaining at the plasma membrane in all time points tested (Fig. 1D/E). Taken together, we find that: (i) KO of P4-ATPase protein complex components reduced aminophospholipid flipping in the plasma membrane of living cells, confirming the functional relevance of the generated cell lines; (ii) P4-ATPases exhibit substrate specificity on the level of lipid species, as P4-ATPase KOs reduce flipping rates for a long-chain PE while the medium-chain PE is unaffected.

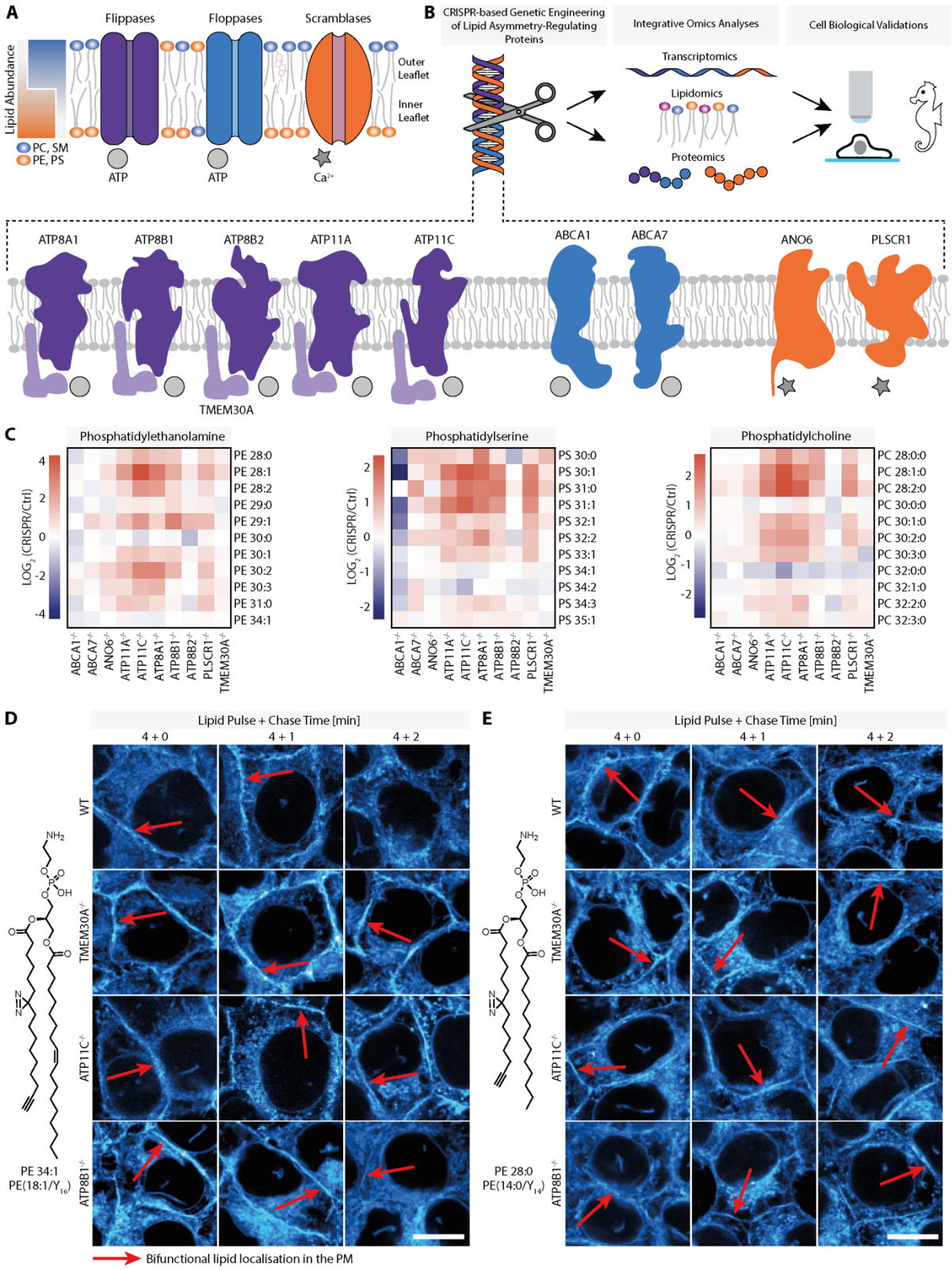

Fig. 1 | Knockout of lipid translocases alters lipid substrate levels and trans-bilayer movement. (**A**) Schematic visualization of lipid asymmetry and its protein machinery. The asymmetric distribution of lipids is generated and maintained by ATP hydrolyzing P_4-ATPases (flippases), ABC transporter (floppases), and dissipated by Ca^{2+} dependent scramblases. The actions of those proteins lead to the characteristic distribution of phosphatidylcholine (PC) and sphingomyelin (SM) to the outer membrane leaflet and phosphatidylethanolamine (PE) and phosphatidylserine (PS) to the inner membrane leaflet of the plasma membrane. (**B**) Experimental

workflow used in this study. Lipid translocases are targeted for CRISPR-mediated gene knockouts. The generated KO cell lines are subjected to bulk transcriptomic, proteomic, and lipidomic analyses. Detected changes are further validated by biochemical and cell biological experiments. (**C**) Detected changes of lipid species across all knockouts (full list of species in extended Data Fig. 3) (**D**) Visualization of retrograde transport of the PE(18:1/Y_{16}) species in WT and KO cell lines via fluorescence microscopy. (**E**) Visualization of retrograde transport of the PE(14:0/Y_{14}) species in WT and KO cell lines via fluorescence microscopy. For (D) and (E) scale bars indicate 10 µm. All images were acquired with the same microscopy settings and were brightness-contrast adjusted in the same manner for better visualization. Red arrows indicate bifunctional lipid localization at the plasma membrane.

Multi-omics analysis uncovers a link between lipid asymmetry and metabolism.

We performed parallel transcriptomic and proteomic analyses in KO versus WT cells to systematically map cellular processes related to plasma membrane lipid asymmetry. RNA sequencing quantified >25000 genes across all conditions (Supplementary Table 1; see Methods). Whole-cell proteomes were acquired using data-independent acquisition mass spectrometry (DIA-MS), and >7000 proteins were quantified across all KO lines after MS quality filtering (4000-5400 proteins per condition; Supplementary Table 2, Extended Data Fig. 5-6). By integrating these datasets, we first sought to gain a global view of changes in cellular processes upon perturbation of the lipid asymmetry machinery. We sorted each dataset into six categories via k-means clustering (Euclidean distance), reflecting the average abundance trends (Fig. 2A). Clusters 4 and 5 featured genes that were up- or down-regulated across all CRISPR lines, respectively (for transcriptomics: average 1.7-fold increase or 1.53-fold decrease; for proteomics: average 1.3-fold increase or 1.15-fold decrease), so we further analyzed these for over-represented gene ontology (GO) terms (Fig. 2A middle panel, Supplemental Table 3). Many GO terms enriched in the transcript and proteome datasets included cellular processes previously linked to plasma membrane lipid asymmetry, expanding the evidence for multiple context-specific studies and giving confidence in our experimental design. Genes with increased abundance (Clusters 4) are involved in cytoskeleton organization, cell adhesion, and membrane trafficking (Fig. 2A), in agreement with the known functions of lipid asymmetry in cell adhesion and migration in mammalian cells[45–49] and membrane trafficking in yeast[50–54]. On the other hand, downregulated genes (Clusters 5) are enriched for GO terms related to cell surface signaling and neurological processes (Supplementary Table 3), reflecting the prevalence of flippase mutations in neurological disorders (e.g., ATP8B1).[36–38] In the transcriptomic data, specifically, the upregulated Cluster 4 also included immune response GO terms, in line with a reported role for ATP11C in B-cell maturation and macrophage function.[55–57]

In addition, we discovered that many of the over-represented GO terms represented numerous aspects of metabolism. This was apparent at both the RNA and protein levels and in both up- and downregulated genes, indicating a multifaceted impact of lipid asymmetry perturbations on cellular metabolism. Specifically, carbohydrate and vitamin transmembrane transport were among the top enriched GO terms for upregulated transcripts, complemented by small molecule metabolism in the proteomics dataset (Clusters 4; Fig. 2A). In gene products with decreased abundance, we found enrichment of numerous GO terms in both datasets for general metabolic pathways ranging from amino acid transport to molecular biosynthesis (e.g., nitrogen compound, nucleobase, heterocycle, amide), macromolecular biosynthesis (DNA, m/r/t/nc/snRNA, peptide), and cellular component biogenesis (Clusters 5; Fig. 2A; Supplemental Table 3). Overall, loss of lipid asymmetry appears to shift the cellular transport of soluble nutrients from amino acids to carbohydrates and induce a corresponding downregulation of macromolecular biosynthesis.

While this general trend is present in all KO lines, we noted that the individual hits passing our significance thresholds differ. Therefore, we analyzed gene-specific trends to narrow down targets and processes for functional follow-ups. First, we found that the most robust changes were caused by KO of P_4-ATPase flippases, in both the pre- and post-thresholded data (Fig. 2B), which also showed high correlation for transcript and protein abundance changes among all family members (Extended Data Fig. 6B). Second, among the genes passing our significance cut-offs in the P_4-ATPase KOs, we found many representative members of the pathways identified by GO enrichment, especially transmembrane solute carriers (SLCs) that were among the top hits in every dataset (Fig. 2C). The broad metabolic regulation was most apparent at the protein level, with common hits including the glucose transporter GLUT1 (SLC2A1; average 3.5-fold increase in ATP11C, ATP8B1 and TMEM30A KOs), the pentose phosphate pathway enzymes glucose-6-phosphate dehydrogenase (G6PD; average 1.7-fold increase) and 6-phosphofructokinase (PFKL; average 1.5-fold increase in ATP8B1 and TMEM30A KOs), and the pyruvate kinase (PKM, average 1.6-fold increase in ATP11C and ATP8B1 KOs) that catalyzes the final rate-limiting step of glycolysis. Similarly, proteins involved in peroxisomal and mitochondrial beta-oxidation, such as the peroxisomal bifunctional enzyme (EHHADH) and the mitochondrial carnitine O-palmitoyltransferase 2 (CPT2), are increased in ATP11C and ATP8B1 KOs (Fig. 2C). Furthermore, the metabolic shift from amino acid to carbohydrate membrane transport is apparent in both data sets as most metabolic GO terms were in the downregulated clusters. Based on these findings, we decided to carry out a mechanistic characterization of the link between maintenance of lipid asymmetry and regulation of cellular metabolism, focusing on the P_4-ATPases.

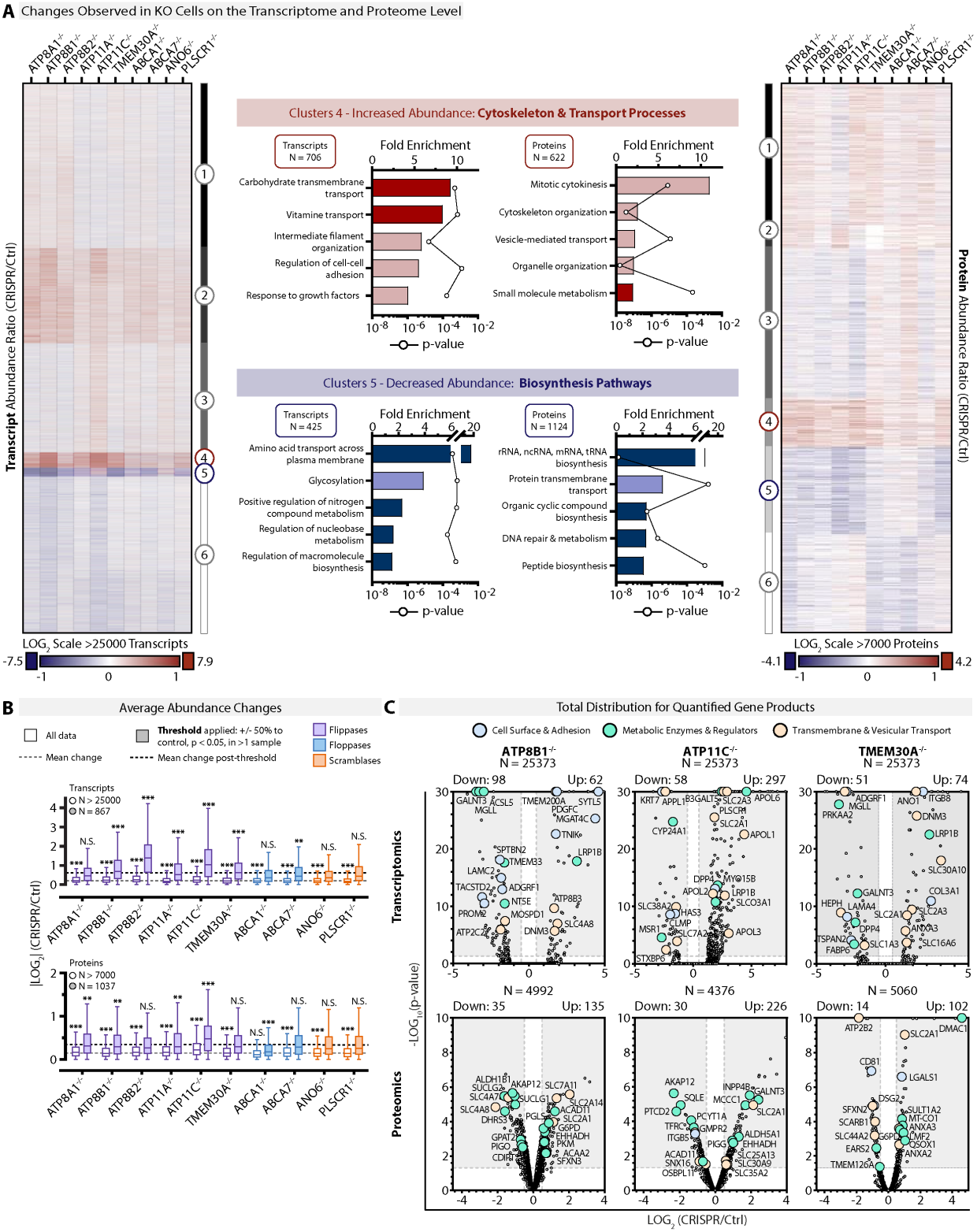

Fig. 2 | Multi-omics analysis reveals a link between lipid asymmetry and energy metabolism. (**A**) Transcriptomic (left heatmap) and proteomic (right heatmap) dataset heatmaps organized by k-means clustering into differentially regulated genes and proteins across all CRISPR KO lines (indicated at top). Color mapping corresponds to the abundance fold-change to WT (Log_2 transformed; key below). Gene ontology (middle panel) statistical over-representation test (PantherDB) for Clusters 4 (upregulated across all CRISPR lines) and 5 (downregulated), showing a selected top 5 umbrella terms for each dataset (see Supplemental Table 3 for complete lists). (**B**) Average abundance changes in complete (white boxes) versus post-statistical thresholding (colored boxes) datasets compared to WT, displayed as a box-and-whisker plot (whiskers are Tukey distribution, box line at median; * $p < 0.05$, ** $p < 0.01$, *** $p < 0.001$, N.S. = non-significant for KO versus all data mean as indicated by dashed

lines). (**C**) Volcano plots showing total data distribution for quantified gene products (top = RNA, lower = protein) for ATP8B1, ATP11C, and TMEM30A KOs. Selected points are highlighted by functional category (color key at top) and the gene name is indicated. Shaded regions represent fold-change to WT ≥2 (x-axis) and $p < 0.05$ (y-axis), with total counts indicated above each graph.

Perturbing lipid asymmetry changes global lipid composition and increases neutral lipid consumption

Among the metabolic hits, we noted that gene products mapping to lipid biosynthesis, beta-oxidation, and lipid droplet maintenance pathways changed in abundance at both the protein and mRNA levels (Fig. 2 & 3A,B). Examples passing our significance cut-offs in multiple KOs include upregulation of the ER-anchored GPI ethanolamine transferase 2 (PIGG; 2-fold average increase), the peroxisomal enoyl-CoA dehydrogenase (EHHADH; 1.8-fold), and the mitochondrial long-chain fatty acid transporter CPT2 (1.5-fold), which were all shared by ATP11C and ATP8B1 KOs. Downregulation of the lipid droplet short-chain dehydrogenase/reductase 3 (DHRS3; average 2.1-fold decrease) was shared between ATP8B1 and TMEM30A KOs, while mitochondrial glycerol-3-phosphate acyltransferase 2 (GPAT2; 1.8-fold decrease) and the ER-anchored very long chain fatty acid elongase 7 (ELOVL7; 1.4-fold decrease) passed significance thresholds in ATP8B1 KO, among others (see Supplemental Table 4 for complete GO-annotated hits in all KO lines). Again, we turned to quantitative shotgun lipidomics to test whether these changes are reflected in cellular lipidome homeostasis. Among various KO-specific trends, we found that PE and its metabolites (lysophosphatidylethanolamine (LPE) and ether lysophosphatidylethanolamine (LPEO)) were elevated in nearly all KOs (Fig. 3C,D and Extended Data Fig. 2C). In contrast, levels of triacylglycerol (TAG) and ether phosphatidylcholine (PCO) decreased. TMEM30A also featured downregulated levels of the second major neutral lipid class, cholesterol esters (Fig. 3D). Increased PE is likely an adaptation to perturbed lipid translocase levels, as aminophospholipids are substrates of P_4-ATPases, which is in-line with our observation that PE internalization was slower upon KO (Fig. 1D). On the other hand, TAGs (decreased) are primary energy storage lipids and major components of lipid droplets, and lysophospholipids (increased) are the side product of fatty acid mobilization from glycerophospholipids. These combined observations suggest an elevated flux of fatty acids towards beta-oxidation for ATP generation. In order to test for altered TAG consumption rates, we conducted an oleic acid feeding experiment, which induces the formation of enlarged lipid droplets. Subsequently, we monitored lipid droplet shrinking by fluorescence microscopy, which indicates neutral lipid consumption. We found that initial lipid droplet formation was significantly reduced in ATP11C KO cells compared to WT, whereas ATP8B1 and TMEM30A KOs exhibited similar trends (Fig. 3 E,F). However, all three KO lines exhibited faster shrinking of lipid droplets after removal of oleic acid (Fig. 3E,F), indicating higher neutral lipid consumption, while maintaining similar number of LDs (Extended Data Fig. 4B). Taken together, our findings suggest that maintenance of lipid asymmetry involves cellular lipid storage pathways.

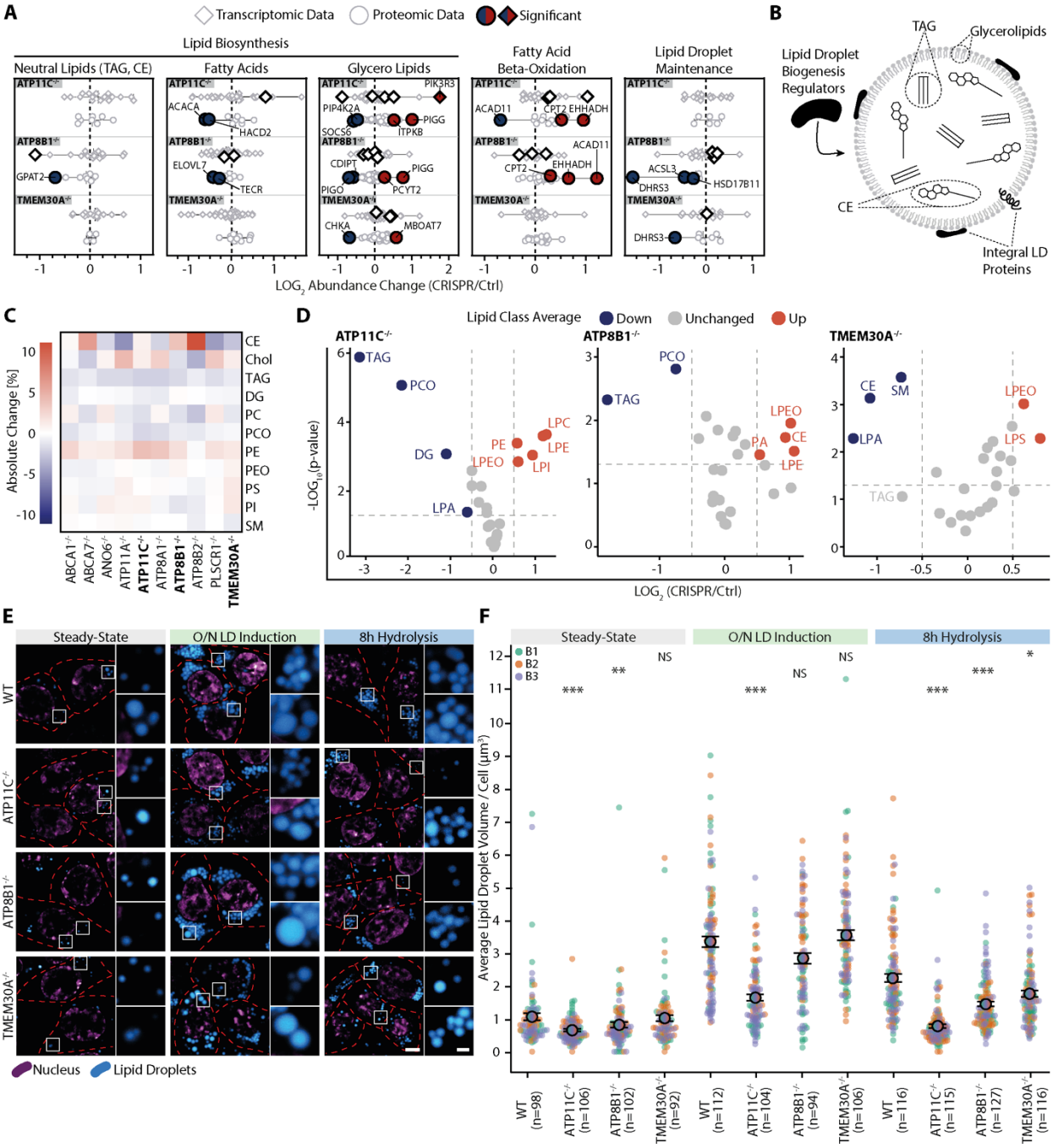

Fig. 3 | Loss of flippase function leads to faster neutral lipid hydrolysis rates. (**A**) Proteins and transcripts related to lipid metabolism are differentially regulated in P_4-ATPase KOs. Plotted are the abundance ratios to control cells (Log_2 scale) for all genes corresponding to that group, sorted by KO line (top to bottom). Each point is an individual gene/protein, with selected genes that pass p<0.05 in at least one omics dataset per KO labeled, enlarged, and colored in the dataset passing significance. See also Supplemental Table 4. (**B**) Schematic overview of lipid droplet (LD) composition. (**C**) Absolute changes in lipid class levels in KO cell lines compared to WT, quantified by lipidomics and shown as a heatmap (key at right). (**D**) Relative changes of lipid levels in ATP11C, ATP8B1 and TMEM30A KO cell lines, shown as a volcano plot (x-axis = ratio to control (Log2 scale); y-axis = p-value; points that pass significance thresholds are colored). (**E**) Assessment of LD hydrolysis in WT versus KO cell lines following overnight (O/N) incubation with oleic acid to induce LD generation. LDs were visualized using LipidSpot, and Hoechst for the nucleus. Red dashed lines indicate cell boundaries, one mid-plane z-slice is shown. Scale bars = 5 µm and 1 µm in the insets. (**F**) Average LD volume per cell, quantified from images as in panel E. All points are shown, colored by biological replicate (B1-B3), with n = number of analyzed cells, p-values above (two-sided Mann-Whitney-U test for each KO compared to WT), and error bars indicating standard error of the mean. p-Values: *** < 0.0001, ** < 0.001, * < 0.01, ns = < 1.

Knockout of P_4-ATPases alters cellular bioenergetics

Our proteomic, transcriptomic, and lipidomic datasets point toward a global change in energy metabolism upon altered lipid trans-bilayer dynamics. Significantly altered gene abundances were observed for major metabolic pathways across subcellular space, including input (transmembrane transport), cytosolic processing (glycolysis, pentose phosphate), and mitochondrial energy output (TCA cycle) (Fig. 4A). Specifically, we found numerous hits related to cellular nutrient uptake by active transmembrane transport, such as GLUT1 (SLC2A1) which we further confirmed by immunofluorescence (Fig. 4B, Extended Data Fig. 7A). The enzymes catalyzing the rate-limiting steps of both the pentose phosphate (glucose-6 phosphate1-dehydrogenase, G6PD; average 1.75-fold increase) and glycolysis (pyruvate kinase, PKM; average 1.6-fold increase) pathways are among the top upregulated proteins across all P_4-ATPase KOs (Fig 4A). Additionally, significant changes are observed for proteins of the TCA cycle (Fig. 4A) and beta-oxidation machinery (Fig. 3A), and decreased TAG levels with elevated neutral lipid consumption (Fig. 3C-F).

We therefore predicted that total cellular bioenergetics were altered upon disruption of lipid asymmetry at the plasma membrane. We used several orthogonal methodologies to characterize the putative changes in global energy metabolism, we used several orthogonal methodologies. First, measurements of steady-state levels of ATP, ADP, and the ATP/ADP ratio showed minor differences between cell lines but no clear trends (Extended Data Fig. 7E). We thus assayed the dynamics of cellular energy metabolism with time-resolved assays. Using a fluorescent ATP biosensor, we found faster ATP depletion kinetics for ATP11C, ATP8B1, and TMEM30A KOs compared to WT after inhibition of both oxidative phosphorylation and glycolysis (Fig. 4C). Furthermore, all tested KO lines exhibited faster oxygen consumption rates (OCR), specifically 50 $\pm$ 2% for ATP11C, 7 $\pm$ 2% for ATP8B1, and 18 $\pm$ 3 % for TMEM30A (Fig. 4D, Extended Data Fig. 7B,C).

Increased metabolic activity could be related to faster cell growth. However, cell counting showed that flippase KOs lines grow slower than WT cells (Fig. 4E). We hypothesized that disruption of lipid asymmetry may lead to an imbalance between cellular energy expenditure and growth, shifting nutrient resources from a more anabolic growth-promoting to a more catabolic energy-consuming metabolic state. Thus, we may expect that the observed metabolic changes in KOs lines lead to elevated energy expenditure per unit biomass grown. To test this, we measured cellular energy expenditure in the form of dissipated heat using isothermal microcalorimetry (Fig. 4F). In parallel, we quantified cellular growth by measurements of total cellular dry mass accumulation using quantitative phase microscopy (Fig. 4G). KO lines showed reduced heat dissipation and biomass accumulation compared to WT cells, which is consistent with our cell-counting results. To investigate whether KO lines expend more energy for growth, we plotted the dissipated heat against the accumulated total cell mass (Fig. 4H, left panel). Using data from the exponential growth phase, we found that heat and mass are linearly correlated for all cell lines measured. The slope quantifies the cellular energy expenditure associated with synthesizing a µg of cellular biomass. Linear regression showed that all KO lines dissipated more heat per biomass than WT cells (Fig. 4H right panel). Similarly, normalizing heat dissipation by total protein content revealed that KO lines dissipated more heat per protein made (Fig. 4I, Extended Data Fig. 7D). These data show that disruption of the lipid asymmetry leads to slower but more energy-consuming cellular growth.

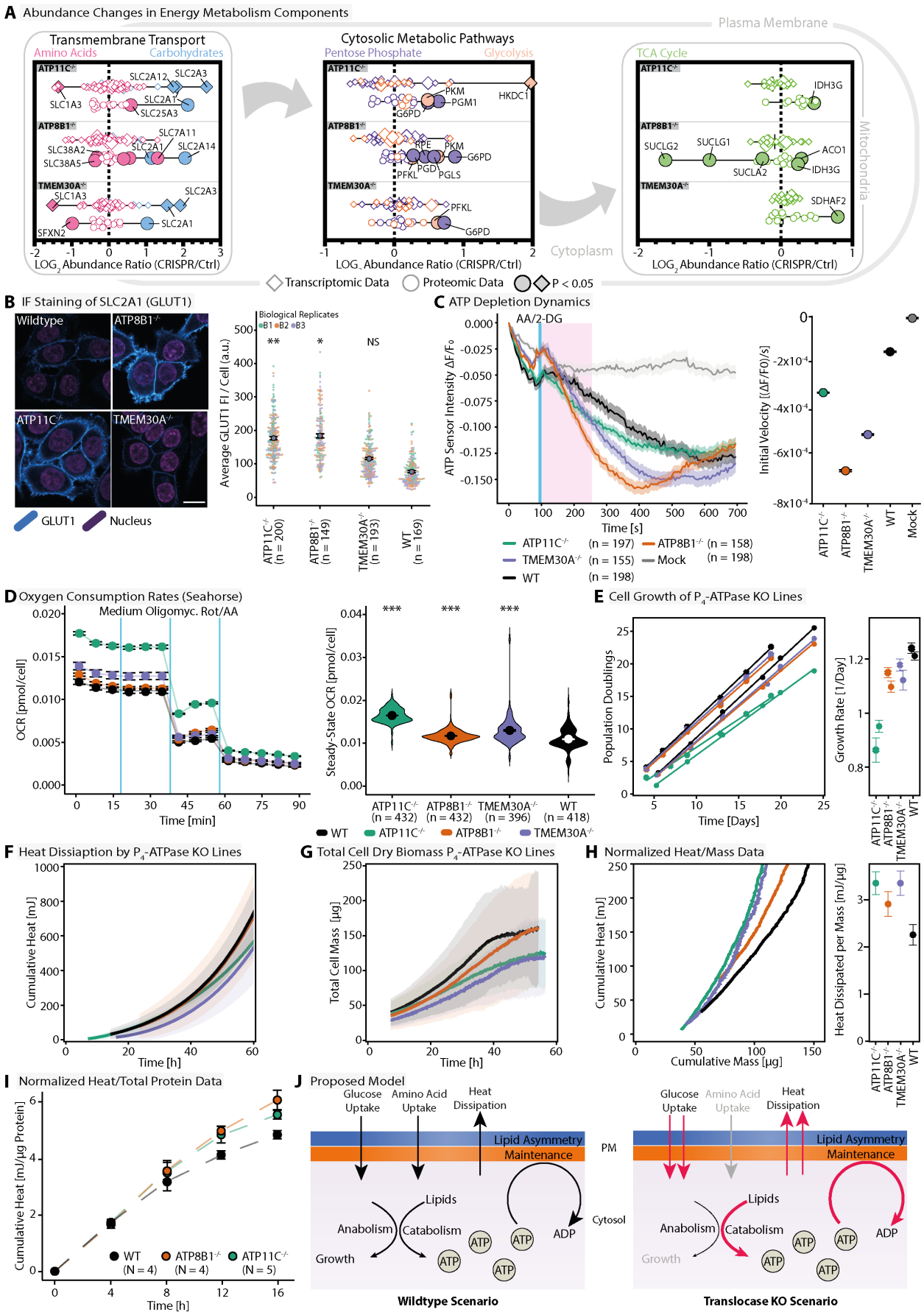
A Abundance Changes in Energy Metabolism Components
Plasma Membrane
Transmembrane Transport
Amino Acids
Carbohydrates
Cytosolic Metabolic Pathways
Pentose Phosphate
Glycolysis
TCA Cycle
Mitochondria
Cytoplasm
LOG2 Abundance Ratio (CRISPR/Ctrl)
Transcriptomic Data
Proteomic Data
P < 0.05
B IF Staining of SLC2A1 (GLUT1)
Wildtype
GLUT1
Nucleus
Biological Replicates
Average GLUT1 FI / Cell (a.u.)
C ATP Depletion Dynamics
AA/2-DG
ATP Sensor Intensity ΔF/F0
Time [s]
Initial Velocity [(ΔF/F0)/s]
D Oxygen Consumption Rates (Seahorse)
Medium Oligomyc. Rot/AA
OCR [pmol/cell]
Time [min]
Steady-State OCR [pmol/cell]
E Cell Growth of P4-ATPase KO Lines
Population Doublings
Time [Days]
Growth Rate [1/Day]
F Heat Dissiaption by P4-ATPase KO Lines
Cumulative Heat [mJ]
Time [h]
G Total Cell Dry Biomass P4-ATPase KO Lines
Total Cell Mass [µg]
H Normalized Heat/Mass Data
Cumulative Mass [µg]
Heat Dissipated per Mass [mJ/µg]
I Normalized Heat/Total Protein Data
Cumulative Heat [mJ/µg Protein]
J Proposed Model
Glucose Uptake
Amino Acid Uptake
Heat Dissipation
Lipid Asymmetry Maintenance
PM
Cytosol
Lipids
Anabolism
Catabolism
Growth
ADP
ATP
Wildtype Scenario
Translocase KO Scenario

Fig. 4 | Loss of flippase function leads to inefficient production of biomass. (**A**) Quantified genes corresponding to major cellular metabolic processes, organized by subcellular location. Each plot is the abundance ratio to control (Log_2 scale) for all genes in the datasets corresponding to that process, sorted by KO line (top to bottom) and colored by pathway. Selected genes that pass $p<0.05$ in at least one omics dataset per KO are labeled, enlarged, and dark-colored for the dataset passing significance. See also Supplemental Table 4. **B**) Immunofluorescence staining of endogenous GLUT1 (SLC2A1) in WT versus KO cells (left panel) and analysis of mean fluorescence intensity (FI) per cell (right panel). Scale bar is 15 µm. Coloured points show single cell measurements (n values given on x-axis) with colours indicating biological replicates, black circles show averages and error bars indicate standard error of the mean. Statistical analysis was performed using Student's t-test for each KO compared to WT. GLUT1 staining of other KO lines can be found in Extended Data Fig. 7A. (**C**) Depletion of cellular ATP measured with a fluorescent ATP sensor (iATPSnFR) after the addition of Antimycin A and 2-Deoxy-D-glucose (2-DG), at the timepoint indicated by the blue line (average traces are shown, n = number of analyzed cells, error bars are standard error of the mean). The area shaded in pink indicate the timeframe used for the calculation of initial velocities (right panel; error bars are standard error of the mean). (**D**) Assessment of cellular oxygen consumption rates (OCRs) via Seahorse assay. Left panel: OCR measurements before and after the addition of Oligomycin and Rotenone (Rot)/Antimycin A (AA), indicated by the blue lines. Right panel: steady-state OCR of the investigated cell lines shown as a violin plot (n = number of total measurements; p-values calculated via two-sided Mann-Whitney-U test of KO versus WT; circle is mean; error bars are standard error of the mean). (**E**) Cell growth expressed in cumulative population doublings, inferred from cell counting during routine passaging (left panel), and corresponding growth rates calculated from linear regression (right panel). Symbols denote two independent batches. Error bars are standard deviation of growth rates bootstrapped distribution with 10000 resamplings. (**F**) Cumulative heat dissipated by KO lines. Shading is standard deviation of 3 biological replicates. (**G**) Total cell dry biomass measured by quantitative phase microscopy. Shading is standard deviation of biological replicates (WT = 5, ATP11C$^{-/-}$ = 4, ATP8B1$^{-/-}$ = 5, TMEM30A$^{-/-}$ = 3). (**H**) Dissipated cumulative heat normalized by cumulative cell dry biomass (time-matched data from Fig. 4F and 4G, left panel). Slopes of linear regression fits of mass-normalized heat data, quantifying the heat dissipation per µg of cell dry biomass grown (right panel). Error bars of right panel are standard deviation of fit slopes bootstrapped distribution with 10000 resamplings including random 20% of original datapoints. (**I**) Cumulative heat dissipated by P_4-ATPase cell lines normalized to total protein as determined by calorimetry (N = number of biological replicates, error bars are standard error of the mean, dashed lines are linear interpolations). (**J**) Schematic representation of altered bioenergetics after disturbance of plasma membrane lipid asymmetry in WT and KO scenarios.
p-Values: *** < 0.0001, ** < 0.001, * < 0.01, ns = < 1.

Discussion

Here, we report a systems-level investigation into the broader biological role of lipid asymmetry in cells. Lipid asymmetry has been previously linked to various specific cellular processes and biophysical properties of cellular membranes. Indeed, we found a number of affected processes previously linked to lipids asymmetry, ranging from immunity[25,26,26,28–30,55–57] over cytoskeleton organization[46] to neurobiology[31–35] (Fig. 2). In addition, we discovered that lipid asymmetry and cellular metabolism are connected by assessing transcriptome, proteome, and lipidome changes caused by genomic perturbation of the protein machinery associated with lipid asymmetry (flippases, floppases and scramblases). While the changes in the cellular lipidome were relatively minor, transcriptomic and proteomic analyses revealed changes in global metabolic GO terms indicating a broader rewiring of cellular metabolism. These over-represented metabolic GO terms were particularly apparent in the P_4-ATPase flippase KO lines. They included down-regulated genes involved in amino-acid uptake, peptide and macromolecular synthesis, and up-regulated genes facilitating carbohydrate and vitamin uptake (Fig. 2). Specifically, upregulation of genes involved in beta-oxidation, carbohydrate uptake, glycolysis and the pentose phosphate pathway (Fig. 3 & 4) was accompanied by faster neutral lipid consumption, increased respiration and ATP usage despite slower cell growth and heat dissipation. Normalization of these multi-faceted metabolic changes to cell growth revealed that cells with perturbed lipid asymmetry are characterized by increased heat dissipation or energy expenditure per unit biomass or protein synthesized. Thus, disruption of

the lipid asymmetry leads to global metabolic and energetics effects that manifest in slower but more energy-consuming cellular growth.

Our data, presented in this work, are consistent with a model that perturbations of plasma membrane lipid asymmetry cause a global rewiring of cellular nutrient uptake, processing, and energy transduction. KOs of flippases lead to a shift from balanced nutrient uptake of sugars and amino acids that supply energy and precursors for anabolic cell growth to reduced amino acid uptake and a more dissipative, energy-consuming, catabolic metabolism fueled by sugars and fats, characterized by slower cell growth (Fig. 4J). Specifically, KO cells dissipate more energy to produce biomass despite slower growth, highlighting a shift from an anabolic to a more catabolic metabolism. Therefore, KO cells might display increased empty cycles by other translocases moving nonoptimal substrates across a concentration gradient to maintain lipid asymmetry, leading to higher ATP consumption and energy dissipation per successful lipid translocation event. Assuming that cells in culture grow at their maximum metabolic capacity, this increased ATP demand to ensure functional asymmetric membranes and viability may come at the cost of reducing other energy-demanding cellular processes. KO cells show down-regulation of genes associated with macromolecule and peptide synthesis and reduced amino acid uptake. This suggests that slower growth results from reduced ribosomal biogenesis and protein translation, which can account for up to 60% of the cellular energy budget in growing cells.[52,53] Thus, the observed global metabolic rewiring is likely a compensatory response that budgets cellular energy expenditure to meet the elevated energy demands for maintaining functional asymmetric membranes by slowing energy-expensive macromolecular synthesis and growth.

Our finding that overall cellular energetics can be affected by the loss of individual flippases initially seems surprising, as it suggests that maintaining baseline lipid asymmetry places significant demands on the cellular energy budget. This is only possible if high rates of active lipid trans-bilayer movement persist at steady state, along with the corresponding ATP hydrolysis rate.

Understanding lipid asymmetry as a highly dynamic phenomenon suggests that its function is not limited to defining the specific material properties of the inner and outer plasma membrane leaflets. It is likely that lipid asymmetry also fulfills a similar role to other transmembrane concentration gradients (ions, protons) as a store of potential energy built by pump-like proteins (flippases) to provide energy required for coupled transmembrane processes. Like uncoupling proteins, channel-like proteins (scramblases) can dissipate the concentration gradients[58], potentially regulating the magnitude of stored energy in asymmetric membranes. This interpretation is supported by membrane reshaping/remodeling observed in response to scrambling during molecular dynamics simulations[58,59] and in-vitro model membrane experiments[60]. We cannot rule out that some solute carrier proteins facilitate nutrient uptake by secondary active transport driven by a gradient of asymmetrically distributed lipids, and that the substantial remodeling of SLC proteome observed in KO cells is an adaptation to a perturbed lipid environment. Furthermore, it has been proposed that lipid translocases drive directional transport of lipids between organelles in combination with bridge-like lipid transfer proteins[61], a model for which we have recently provided further experimental evidence[42]. This in turn would mean that the asymmetric lipid distribution of the late secretory pathway organelles could be the energy reservoir required for directional non-vesicular lipid transport between organelle membranes, which is increasingly seen as the primary process for maintaining functional organelle lipid

compositions[42]. Taken together, our findings pave the way towards linking the fields of lipid asymmetry, lipid transport and organelle membrane identity and cellular bioenergetics.

Author Contributions

PB and AN conceptualized and designed the project. AS, JR and AN supervised the project. PB prepared figures with contributions from KCC, VB and SMK. PB prepared samples for all omics analyses with contribution from SMK. TJ performed proteomics experiments. KCC, PB, TJ and AN analyzed transcriptomic and proteomic data. KB synthesized lipid probes. HML performed lipid imaging experiments. KS performed lipidomics experiments. KS and PB analyzed lipidomics data. PB, SMK and CJM performed fluorescence microscopy experiments. PB analyzed fluorescence microscopy data with contribution of SMK. PB performed Seahorse assays. PB and TCA analyzed Seahorse data. ST performed ATP/ADP measurements. ST and PB analyzed ATP/ADP data. VB performed the quantitative phase microscopy experiments and analyzed data. PB, VB and JR performed calorimetry experiments and analyzed data. PB and AN wrote the manuscript with contribution of KCC, VB and JR. All authors read and commented on the manuscript.

Acknowledgements

This work was supported by the Max Planck Society. AN and JR gratefully acknowledge financial support by the European Research Council (ERC) under the European Union's Horizon 2020 research and innovation program (grant agreements no GA 758334 ASYMMEM and GA 949811 EnBioSys). AN and AS acknowledge financial support by the Deutsche Forschungsgemeinschaft (DFG) via the TRR83 consortium. This research was supported by an Allen Distinguished Investigator Award, a Paul G. Allen Frontiers Group advised grant of the Paul G. Allen Family Foundation to AN. We thank the following services and facilities at MPI-CBG Dresden for their support: Protein Expression Facility, Scientific Computing Facility, Genome Engineering Facility, Technology Development Studio and the Light Microscopy Facility. Furthermore, we would like to thank the Genome Center at CRTD/CMCB for their support.

Conflict of interest

The authors declare no conflict of interest.

Code and data availability

All data and code used in this study can be assessed on the following repository: EDMOND (https://doi.org/10.17617/3.1HISIJ).

References

1. Verkleij, A. J. *et al.* The asymmetric distribution of phospholipids in the human red cell membrane. A combined study using phospholipases and freeze-etch electron microscopy. *Biochim. Biophys. Acta BBA - Biomembr.* **323**, 178–193 (1973).
2. Lorent, J. H. *et al.* Plasma membranes are asymmetric in lipid unsaturation, packing and protein shape. *Nat. Chem. Biol.* **16**, 644–652 (2020).
3. Devaux, P. F. Static and dynamic lipid asymmetry in cell membranes. *Biochemistry* **30**, 1163–1173 (1991).
4. Doktorova, M., Symons, J. L. & Levental, I. Structural and functional consequences of reversible lipid asymmetry in living membranes. *Nat. Chem. Biol.* **16**, 1321–1330 (2020).
5. Pomorski, T. & Menon, A. K. Lipid flippases and their biological functions. *Cell. Mol. Life Sci.* **63**, 2908–2921 (2006).
6. Doktorova, M. *et al.* Cell membranes sustain phospholipid imbalance via cholesterol asymmetry. *Cell*, (2025), https://doi.org/10.1016/j.cell.2025.02.034.
7. Holthuis, J. C. M. & Menon, A. K. Lipid landscapes and pipelines in membrane homeostasis. *Nature* **510**, 48–57 (2014).
8. Kobayashi, T. & Menon, A. K. Transbilayer lipid asymmetry. *Curr. Biol.* **28**, R386–R391 (2018).
9. Lopez-Marques, R. L., Theorin, L., Palmgren, M. G. & Pomorski, T. G. P4-ATPases: lipid flippases in cell membranes. *Pflüg. Arch. - Eur. J. Physiol.* **466**, 1227–1240 (2014).
10. Pomorski, T. G. & Menon, A. K. Lipid somersaults: Uncovering the mechanisms of protein-mediated lipid flipping. *Prog. Lipid Res.* **64**, 69–84 (2016).
11. Falzone, M. E. *et al.* Structural basis of Ca2+-dependent activation and lipid transport by a TMEM16 scramblase. *eLife* **8**, e43229 (2019).

12. Malvezzi, M. *et al.* Ca2+-dependent phospholipid scrambling by a reconstituted TMEM16 ion channel. *Nat. Commun.* **4**, 2367 (2013).

13. Kalienkova, V., Clerico Mosina, V. & Paulino, C. The Groovy TMEM16 Family: Molecular Mechanisms of Lipid Scrambling and Ion Conduction. *J. Mol. Biol.* **433**, 166941 (2021).

14. Hammill, A. K., Uhr, J. W. & Scheuermann, R. H. Annexin V Staining Due to Loss of Membrane Asymmetry Can Be Reversible and Precede Commitment to Apoptotic Death. *Exp. Cell Res.* **251**, 16–21 (1999).

15. Shin, H.-W. & Takatsu, H. Phosphatidylserine exposure in living cells. *Crit. Rev. Biochem. Mol. Biol.* **55**, 166–178 (2020).

16. van den Eijnde, S. M. *et al.* Transient expression of phosphatidylserine at cell-cell contact areas is required for myotube formation. *J. Cell Sci.* **114**, 3631–3642 (2001).

17. Jeong, J. & Conboy, I. M. Phosphatidylserine directly and positively regulates fusion of myoblasts into myotubes. *Biochem. Biophys. Res. Commun.* **414**, 9–13 (2011).

18. Park, S.-Y. *et al.* Stabilin-2 modulates the efficiency of myoblast fusion during myogenic differentiation and muscle regeneration. *Nat. Commun.* **7**, 10871 (2016).

19. Tsuchiya, M. *et al.* Cell surface flip-flop of phosphatidylserine is critical for PIEZO1-mediated myotube formation. *Nat. Commun.* **9**, 2049 (2018).

20. de Vries, K. J., Wiedmer, T., Sims, P. J. & Gadella, B. M. Caspase-Independent Exposure of Aminophospholipids and Tyrosine Phosphorylation in Bicarbonate Responsive Human Sperm Cells1. *Biol. Reprod.* **68**, 2122–2134 (2003).

21. Rival, C. M. *et al.* Phosphatidylserine on viable sperm and phagocytic machinery in oocytes regulate mammalian fertilization. *Nat. Commun.* **10**, 4456 (2019).

22. Zhang, Y. *et al.* TMEM16F phospholipid scramblase mediates trophoblast fusion and placental development. *Sci. Adv.* **6**, eaba0310 (2020).

23. Lentz, B. R. Exposure of platelet membrane phosphatidylserine regulates blood coagulation. *Prog. Lipid Res.* **42**, 423–438 (2003).

24. Reddy, E. C. & Rand, M. L. Procoagulant Phosphatidylserine-Exposing Platelets in vitro and in vivo. *Front. Cardiovasc. Med.* **7**, (2020).

25. Elliott, J. I. *et al.* Membrane phosphatidylserine distribution as a non-apoptotic signalling mechanism in lymphocytes. *Nat. Cell Biol.* **7**, 808–816 (2005).

26. Bleibaum, F. *et al.* ADAM10 sheddase activation is controlled by cell membrane asymmetry. *J. Mol. Cell Biol.* **11**, 979–993 (2019).

27. Sommer, A. *et al.* Phosphatidylserine exposure is required for ADAM17 sheddase function. *Nat. Commun.* **7**, 11523 (2016).

28. Fischer, K. *et al.* Antigen recognition induces phosphatidylserine exposure on the cell surface of human CD8+ T cells. *Blood* **108**, 4094–4101 (2006).

29. Stowell, S. R. *et al.* Galectin-1 Induces Reversible Phosphatidylserine Exposure at the Plasma Membrane. *Mol. Biol. Cell* **20**, 1408–1418 (2009).

30. Connolly, A. *et al.* TMEM16F mediates bystander TCR-CD3 membrane dissociation at the immunological synapse and potentiates T cell activation. *Sci. Signal.* **14**, eabb5146 (2021).

31. Levano, K. *et al.* Atp8a1 deficiency is associated with phosphatidylserine externalization in hippocampus and delayed hippocampus-dependent learning. *J. Neurochem.* **120**, 302–313 (2012).

32. Scott-Hewitt, N. *et al.* Local externalization of phosphatidylserine mediates developmental synaptic pruning by microglia. *EMBO J.* **39**, e105380 (2020).

33. Li, T. *et al.* Phospholipid-flippase chaperone CDC50A is required for synapse maintenance by regulating phosphatidylserine exposure. *EMBO J.* **40**, e107915 (2021).

34. Hisamoto, N. *et al.* Phosphatidylserine exposure mediated by ABC transporter activates the integrin signaling pathway promoting axon regeneration. *Nat. Commun.* **9**, 3099 (2018).

35. Ruggiero, L., Connor, M. P., Chen, J., Langen, R. & Finnemann, S. C. Diurnal, localized exposure of phosphatidylserine by rod outer segment tips in wild-type but not Itgb5−/− or Mfge8−/− mouse retina. *Proc. Natl. Acad. Sci.* **109**, 8145–8148 (2012).

36. Stapelbroek, J. M. *et al.* ATP8B1 is essential for maintaining normal hearing. *Proc. Natl. Acad. Sci.* **106**, 9709–9714 (2009).

37. Verhulst, P. M. *et al.* A flippase-independent function of ATP8B1, the protein affected in familial intrahepatic cholestasis type 1, is required for apical protein expression and microvillus formation in polarized epithelial cells. *Hepatology* **51**, 2049–2060 (2010).

38. Korneenko, T. V., Pestov, N. B., Okkelman, I. A., Modyanov, N. N. & Shakhparonov, M. I. P4-ATPase Atp8b1/FIC1: Structural features and physiological functions in health and disease. *Russ. J. Bioorganic Chem.* **41**, 1–9 (2015).

39. Castoldi, E., Collins, P. W., Williamson, P. L. & Bevers, E. M. Compound heterozygosity for 2 novel TMEM16F mutations in a patient with Scott syndrome. *Blood* **117**, 4399–4400 (2011).

40. Doktorova, M., Levental, I. & Heberle, F. A. Seeing the Membrane from Both Sides Now: Lipid Asymmetry and Its Strange Consequences. *Cold Spring Harb. Perspect. Biol.* **15**, a041393 (2023).

41. Ezanno, P., Cribier, S. & Devaux, P. F. Asymmetrical stress generated by the erythrocyte lipid flippase triggers multiple bud formation on the surface of spherical giant liposomes. *Eur. Biophys. J.* **39**, 1277–1280 (2010).

42. Iglesias-Artola, J. M. *et al.* Quantitative imaging of species-specific lipid transport in mammalian cells. 2024.05.14.594078 Preprint at https://doi.org/10.1101/2024.05.14.594078 (2024).

43. Bryde, S. *et al.* CDC50 Proteins Are Critical Components of the Human Class-1 P4-ATPase Transport Machinery *. *J. Biol. Chem.* **285**, 40562–40572 (2010).

44. Lenoir, G., Williamson, P., Puts, C. F. & Holthuis, J. C. M. Cdc50p Plays a Vital Role in the ATPase Reaction Cycle of the Putative Aminophospholipid Transporter Drs2p *♦. *J. Biol. Chem.* **284**, 17956–17967 (2009).

45. Schlegel, R. A., Prendergast, T. W. & Williamson, P. Membrane phospholipid asymmetry as a factor in erythrocyte-endothelial cell interactions. *J. Cell. Physiol.* **123**, 215–218 (1985).

46. Manno, S., Takakuwa, Y. & Mohandas, N. Identification of a functional role for lipid asymmetry in biological membranes: Phosphatidylserine-skeletal protein interactions modulate membrane stability. *Proc. Natl. Acad. Sci.* **99**, 1943–1948 (2002).

47. Jacobsen, K. S. *et al.* The role of TMEM16A (ANO1) and TMEM16F (ANO6) in cell migration. *Pflüg. Arch. - Eur. J. Physiol.* **465**, 1753–1762 (2013).

48. Panatala, R., Hennrich, H. & Holthuis, J. C. M. Inner workings and biological impact of phospholipid flippases. *J. Cell Sci.* **128**, 2021–2032 (2015).

49. Bricogne, C. *et al.* TMEM16F activation by Ca2+ triggers plasma membrane expansion and directs PD-1 trafficking. *Sci. Rep.* **9**, 619 (2019).

50. Chen, C.-Y., Ingram, M. F., Rosal, P. H. & Graham, T. R. Role for Drs2p, a P-Type Atpase and Potential Aminophospholipid Translocase, in Yeast Late Golgi Function. *J. Cell Biol.* **147**, 1223–1236 (1999).

51. Pomorski, T. *et al.* Drs2p-related P-type ATPases Dnf1p and Dnf2p Are Required for Phospholipid Translocation across the Yeast Plasma Membrane and Serve a Role in Endocytosis. *Mol. Biol. Cell* **14**, 1240–1254 (2003).

52. Barbosa, S., Pratte, D., Schwarz, H., Pipkorn, R. & Singer-Krüger, B. Oligomeric Dop1p is Part of the Endosomal Neo1p-Ysl2p-Arl1p Membrane Remodeling Complex. *Traffic* **11**, 1092–1106 (2010).

53. Das, A. *et al.* Flippase-mediated phospholipid asymmetry promotes fast Cdc42 recycling in dynamic maintenance of cell polarity. *Nat. Cell Biol.* **14**, 304–310 (2012).

54. Takeda, M., Yamagami, K. & Tanaka, K. Role of Phosphatidylserine in Phospholipid Flippase-Mediated Vesicle Transport in Saccharomyces cerevisiae. *Eukaryot. Cell* **13**, 363–375 (2014).

55. Yabas, M. *et al.* ATP11C is critical for the internalization of phosphatidylserine and differentiation of B lymphocytes. *Nat. Immunol.* **12**, 441–449 (2011).

56. Siggs, O. M. *et al.* The P4-type ATPase ATP11C is essential for B lymphopoiesis in adult bone marrow. *Nat. Immunol.* **12**, 434–440 (2011).

57. Segawa, K. *et al.* Phospholipid flippases enable precursor B cells to flee engulfment by macrophages. *Proc. Natl. Acad. Sci.* **115**, 12212–12217 (2018).

58. Siggel, M., Bhaskara, R. M. & Hummer, G. Phospholipid Scramblases Remodel the Shape of Asymmetric Membranes. *J. Phys. Chem. Lett.* **10**, 6351–6354 (2019).

59. Bennett, W. F. D. & Tieleman, D. P. Molecular simulation of rapid translocation of cholesterol, diacylglycerol, and ceramide in model raft and nonraft membranes. *J. Lipid Res.* **53**, 421–429 (2012).

60. Papadopulos, A. *et al.* Flippase Activity Detected with Unlabeled Lipids by Shape Changes of Giant Unilamellar Vesicles*. *J. Biol. Chem.* **282**, 15559–15568 (2007).

61. Ghanbarpour, A., Valverde, D. P., Melia, T. J. & Reinisch, K. M. A model for a partnership of lipid transfer proteins and scramblases in membrane expansion and organelle biogenesis. *Proc. Natl. Acad. Sci.* **118**, e2101562118 (2021).

Extended Data Figures

Disruption of Plasma Membrane Lipid Asymmetry Alters Cellular Energetics

Authors: Pavel Barahtjan[1,2], Katelyn C. Cook[1], Václav Bočan[1], H. Mathilda Lennartz[1], Tobias Jumel[1], Kai Schuhmann[1], Sofia Traikov[3], Kristin Böhlig[1], Sascha M. Kuhn[1], Cristina Jiménez López[1], Tiago C. Alves[3,4], Andrej Shevchenko[1], Jonathan Rodenfels[1,5]* & André Nadler[1]*

Affiliations:
[1]Max-Planck-Institute of Molecular Cell Biology and Genetics, Dresden, 01307, Germany
[2]Interfaculty Institute of Bioengineering and Global Health Institute, École Polytechnique Fédérale de Lausanne (EPFL), Lausanne, 1015, Switzerland
[3]Institute for Clinical Chemistry and Laboratory Medicine, Universitätsklinikum Carl Gustav Carus, Technical University Dresden, Germany
[4]DZD-Paul Langerhans Institute of the Helmholtz Zentrum München, Germany
[5]Cluster of Excellence Physics of Life, Technical University Dresden, Dresden, Germany

*Corresponding authors. Email: rodenfels@mpi-cbg.de & nadler@mpi-cbg.de

Extended Data Figures

A

ABCA1 Gene Exons (partially)

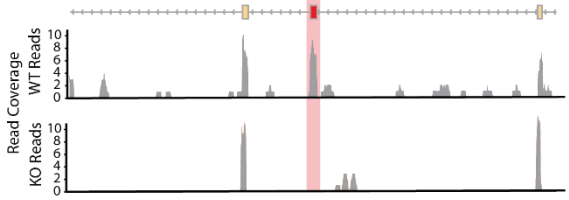

ABCA7 Gene Exons (partially)

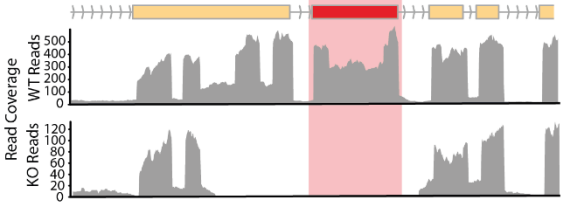

ANO6 Gene Exons (partially)

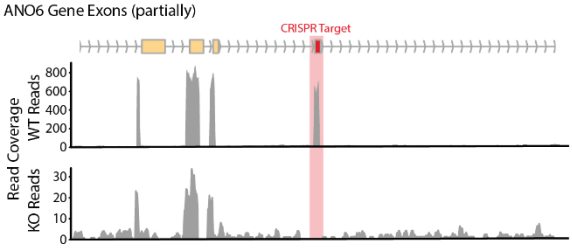

ATP8A1 Gene Exons (partially)

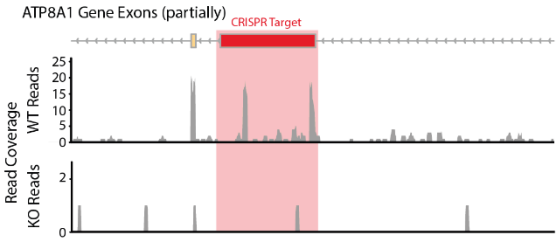

ATP8B1 Gene Exons (partially)

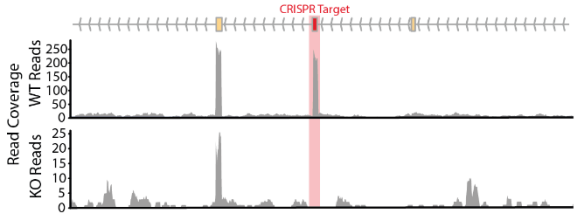

ATP8B2 Gene Exons (partially)

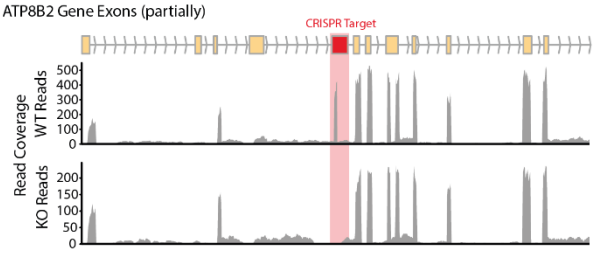

ATP11C Gene Exons (partially)

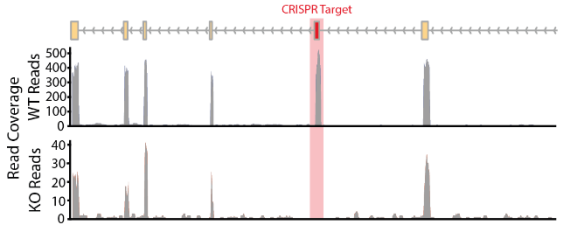

TMEM30A Gene Exons (partially)

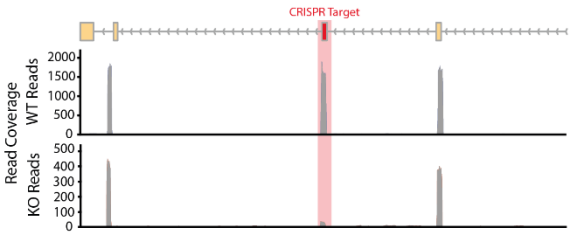

B

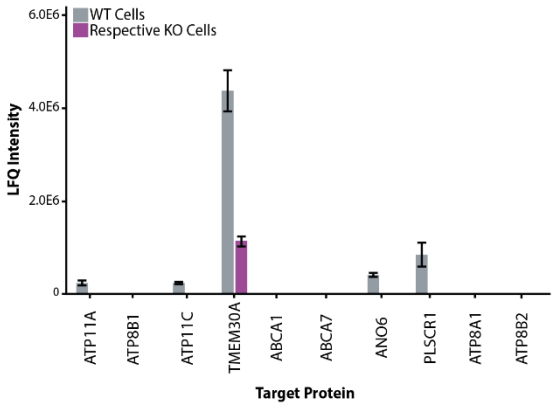

Extended Data Fig. 1 | Confirmation of the successful deletion of the target exon. (**A**) Read coverage of the partial gene regions for all KO targets that were close to the targeted exon. WT and KO reads of the respective regions are shown and the red bar indicates the targeted exon for deletion. (**B**) Proteomic assessment of targeted proteins for KO. For ATP11A, ATP11C, TMEM30A, ANO6 and PLSCR1 protein was detected in the WT cells (grey bar) and the amount of protein detected in the respective KO shown in violet. Error bars indicate standard error of the mean.

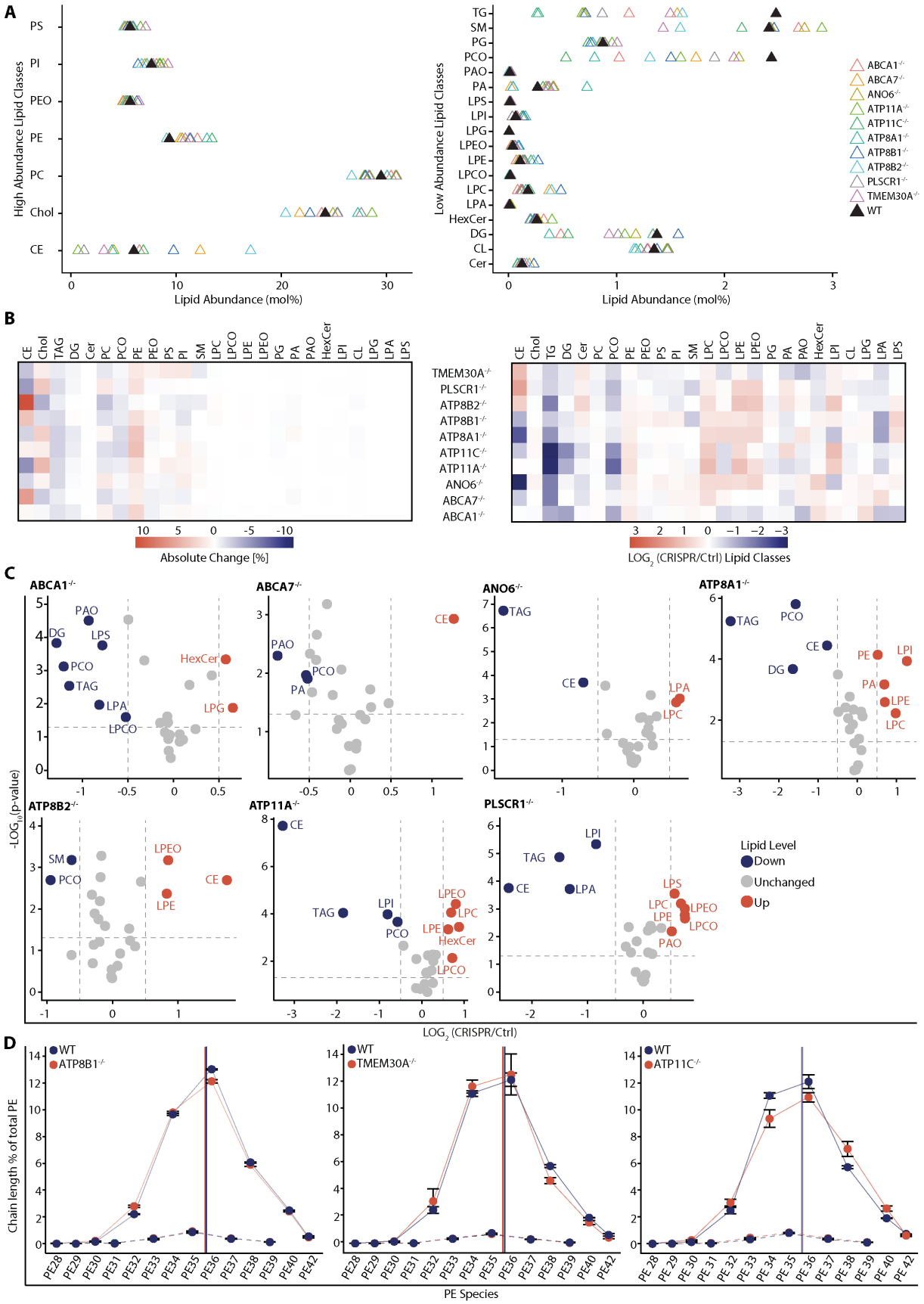
A
High Abundance Lipid Classes
PS
PI
PEO
PE
PC
Chol
CE
Lipid Abundance (mol%)
Low Abundance Lipid Classes
TG
SM
PG
PCO
PAO
PA
LPS
LPI
LPG
LPEO
LPE
LPCO
LPC
LPA
HexCer
DG
CL
Cer
ABCA1-/-
ABCA7-/-
ANO6-/-
ATP11A-/-
ATP11C-/-
ATP8A1-/-
ATP8B1-/-
ATP8B2-/-
PLSCR1-/-
TMEM30A-/-
WT
B
Absolute Change [%]
LOG2 (CRISPR/Ctrl) Lipid Classes
C
ABCA1-/-
ABCA7-/-
ANO6-/-
ATP8A1-/-
ATP8B2-/-
ATP11A-/-
PLSCR1-/-
-LOG10(p-value)
LOG2 (CRISPR/Ctrl)
Lipid Level
Down
Unchanged
Up
D
WT
ATP8B1-/-
TMEM30A-/-
ATP11C-/-
Chain length % of total PE
PE Species

Extended Data Fig. 2 | Analysis of shotgun lipidomics data. (**A**) Overall lipid composition of the investigated cells. (**B**) Extended data for Fig. 3C. All absolute and relative lipid changes of KO cell lines in comparison to WT cells. (**C**) Extended data for Fig. 3D. Relative lipid changes in the knockout cells compared to the WT cells. (**D**) Average chain-length of all detected PE species as shown for WT, ATP11C$^{-/-}$ and TMEM30A$^{-/-}$ KOs.

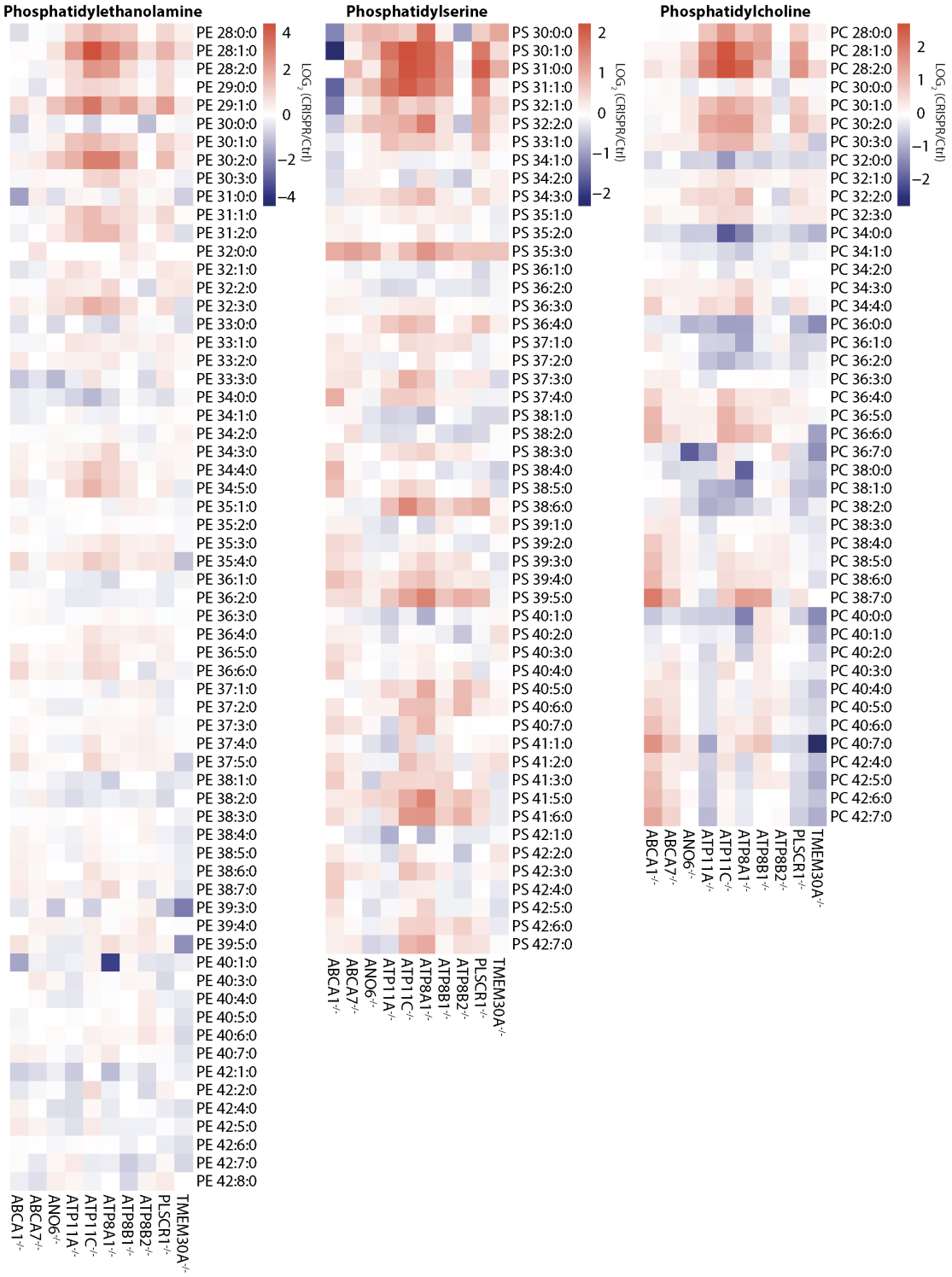

Extended Data Fig. 3 | Observed lipid species changes of PE, PS and PC. Relative changes on lipid species levels of PE, PS and PC in KO cells compared to WT. Extended data for Fig. 1C.

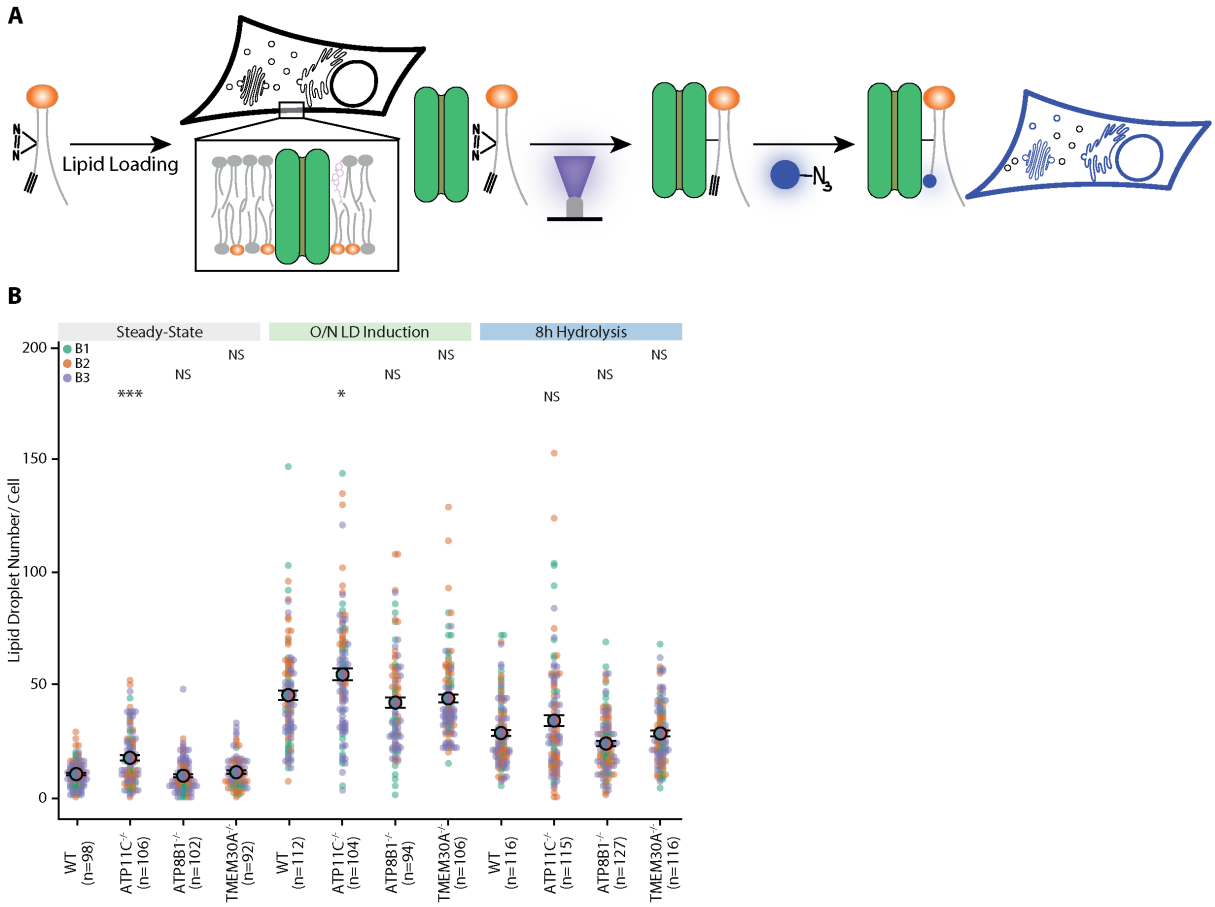

Extended Data Fig. 4| Lipid imaging workflow and lipid droplet quantification. (A) Schematic representation of the lipid imaging workflow. Bifunctional lipids were loaded into the plasma membrane of cells via alpha-methyl-cyclodextrin mediated lipid exchange. After a 4 min pulse, the lipid loading solution was removed and intracellular bifunctional lipids were crosslinked after defined chase time using UV light. Cells were chemically fixed immediately afterwards and covalent lipid protein conjugates fluorescently labelled using chemistry, followed by fluorescence microscopy. (**B**) Average LD number per cell for the oleic acid feeding experiment shown in Fig. 3E. Average LD number per cell. Data points are colored by biological replicate (B1-B3), with n = number of analyzed cells, p-values derived from a two-sided Mann-Whitney-U test for each KO compared to WT, and error bars indicating standard error of the mean. p-Values: *** < 0.0001, ** < 0.001, * < 0.01, ns = < 1.

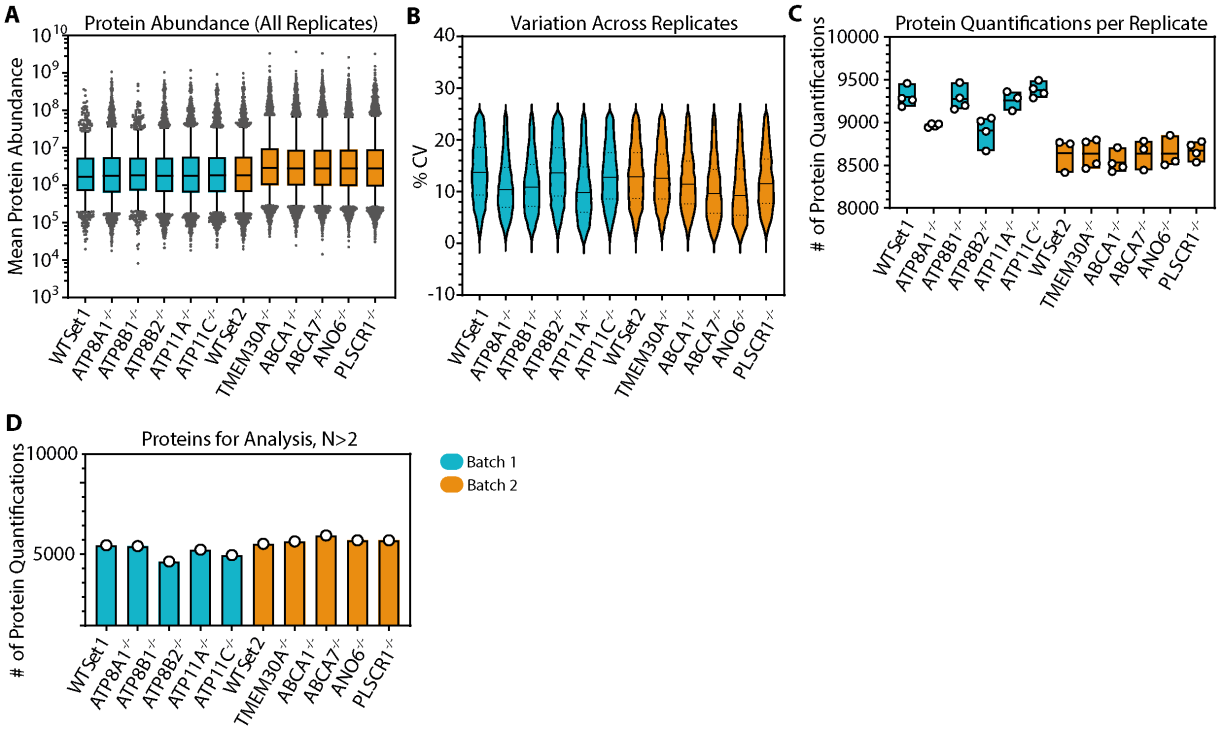

Extended Data Fig. 5 | MS detection and quantification representations for proteomics datasets. (**A**) Mean peptide intensity for proteins detected and quantified by DIA LC-MS/MS, prior to %CV filtering (FDR < 1% for all included peptide values). Data is depicted as box-and-whiskers with 10-90% confidence intervals, line at median, and dots for remaining protein values. (**B**) Coefficient of variation (%CV) across all replicates for all proteomics data included in this study (N=4 biological replicates total, gathered in two separate batches for each CRISPR line). Shown as violin plots for the full range of data, with solid line and median and dotted lines at quartiles. (**C**) Number of protein quantifications per replicate for each CRISPR cell line, prior to %CV or replicate completeness filtering (FDR <1%). Each dot indicates a replicate and the box shows the min/max with solid line at the median. (**D**) Protein abundance values used for all analyses in all main and supplementary figures in this study were filtered for CV < 25% and data completeness in N>2 biological replicates.

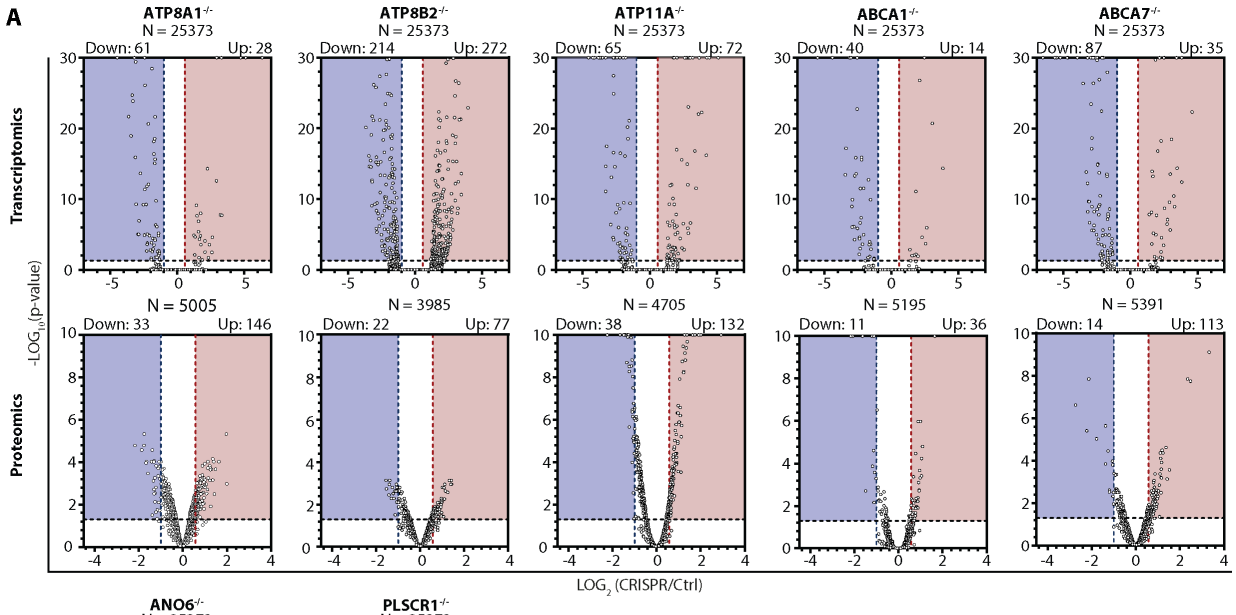
A
ATP8A1-/-
N = 25373
Down: 61
Up: 28
ATP8B2-/-
N = 25373
Down: 214
Up: 272
ATP11A-/-
N = 25373
Down: 65
Up: 72
ABCA1-/-
N = 25373
Down: 40
Up: 14
ABCA7-/-
N = 25373
Down: 87
Up: 35
Transcriptomics
N = 5005
Down: 33
Up: 146
N = 3985
Down: 22
Up: 77
N = 4705
Down: 38
Up: 132
N = 5195
Down: 11
Up: 36
N = 5391
Down: 14
Up: 113
Proteomics
-LOG10(p-value)
LOG2 (CRISPR/Ctrl)

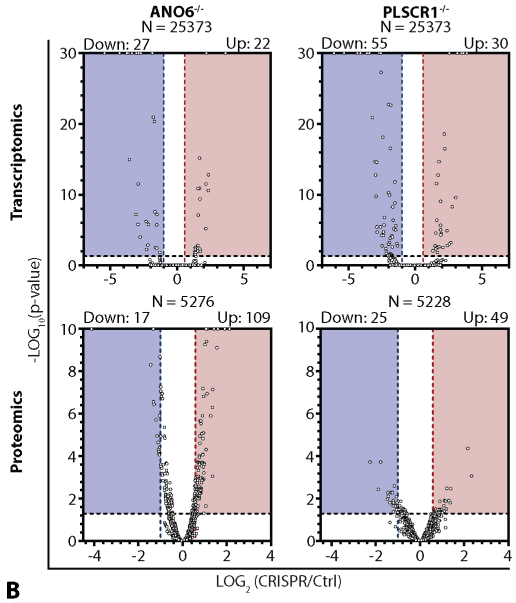
ANO6-/-
N = 25373
Down: 27
Up: 22
PLSCR1-/-
N = 25373
Down: 55
Up: 30
Transcriptomics
N = 5276
Down: 17
Up: 109
N = 5228
Down: 25
Up: 49
Proteomics
-LOG10(p-value)
LOG2 (CRISPR/Ctrl)

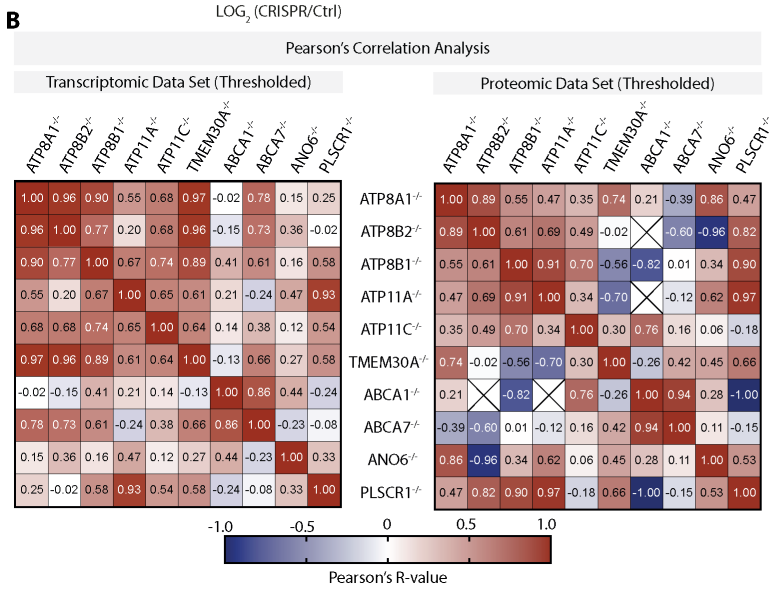
B
Pearson's Correlation Analysis
Transcriptomic Data Set (Thresholded)
Proteomic Data Set (Thresholded)
ATP8A1-/-
ATP8B2-/-
ATP8B1-/-
ATP11A-/-
ATP11C-/-
TMEM30A-/-
ABCA1-/-
ABCA7-/-
ANO6-/-
PLSCR1-/-
-1.0
-0.5
0
0.5
1.0
Pearson's R-value

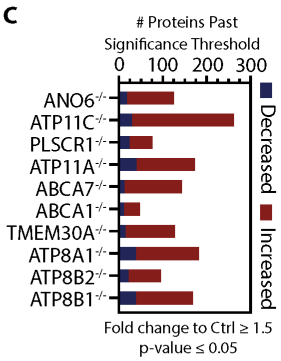
C
Proteins Past
Significance Threshold
0
100
200
300
ANO6-/-
ATP11C-/-
PLSCR1-/-
ATP11A-/-
ABCA7-/-
ABCA1-/-
TMEM30A-/-
ATP8A1-/-
ATP8B2-/-
ATP8B1-/-
Decreased
Increased
Fold change to Ctrl ≥ 1.5
p-value ≤ 0.05

Extended Data Fig. 6 | Transcript and protein abundances are differentially modulated by CRISPR KO of plasma membrane lipid asymmetry-associated proteins. (**A**) Volcano plots showing the full data distribution for transcriptomics (top panels) and proteomics (lower panels) analyses in CRISPR knockout lines (genes indicated above graphs; ATP8B1, APT11C, and TMEM30A volcano plots are in Figure 2). Shaded regions represent fold-change to wildtype ≥2 (x-axis) and $p < 0.05$ (y-axis), and each dot represents a transcript/protein, with total counts indicated above each graph. Data included here is already filtered for transcriptomic and proteomic quality as described in Methods. (**B**) Data correlation matrices showing Pearson's Correlation R values for each pair of CRISPR KOs in the transcriptomic (left) and proteomic (right) data for significantly regulated gene products only (thresholded by +/-50% change to control, $p < 0.05$; N = 867 transcripts and N = 1037 proteins). R values for each comparison are written in each cell. (**C**) Number of proteins passing significance thresholds for each CRISPR condition. For all CRISPR cell lines, the number of significantly increased protein abundances (red bars) superseded the number decreased (blue bars), and the total (sum of stacked bars) varied across CRISPR conditions.

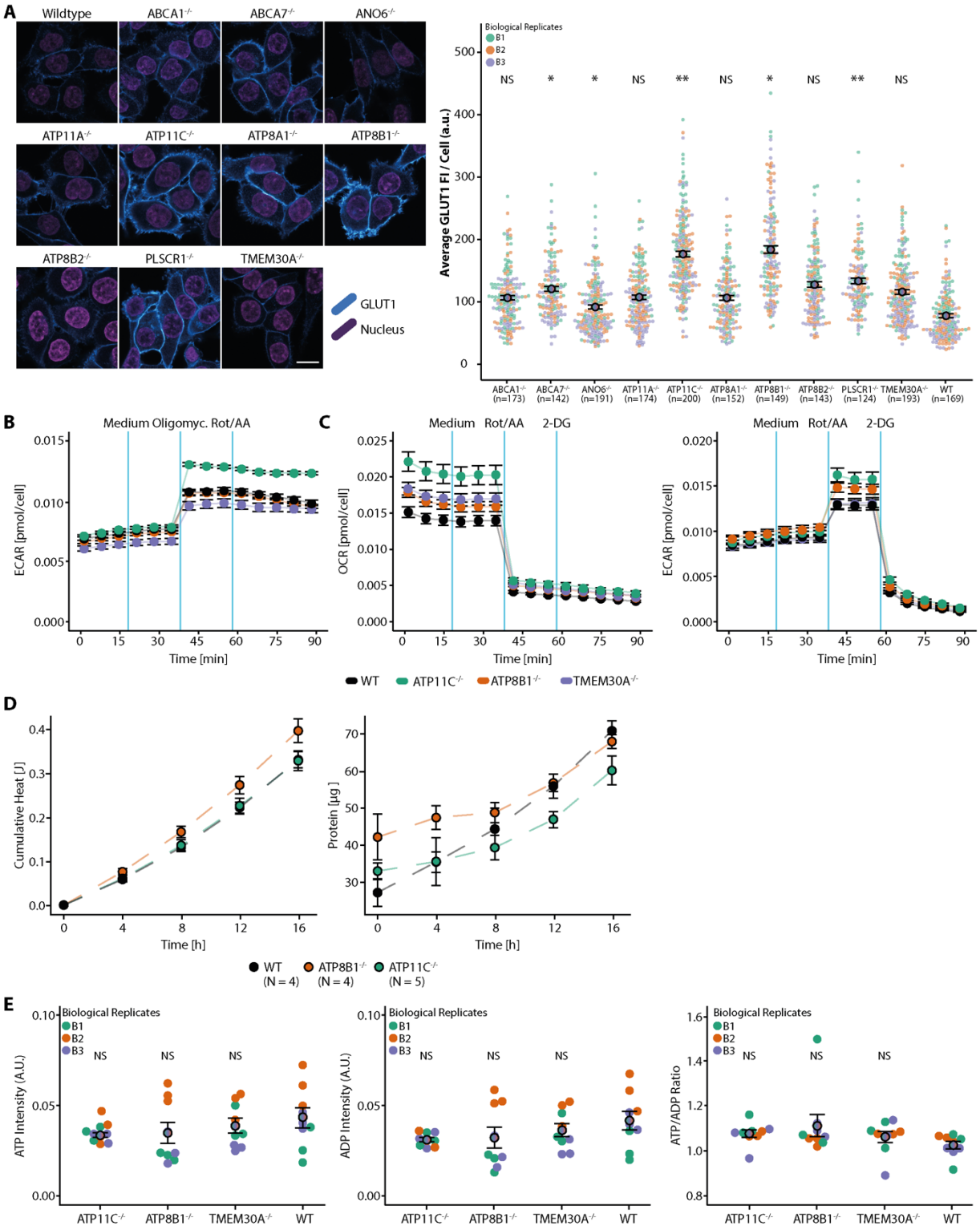

Extended Data Fig. 7 | KO cell lines exhibit altered bioenergetics. (A) Immunofluorescence staining of GLUT1 in selected KO cell lines (left panel) and analysis of mean fluorescence intensity (FI) per cell (right panel). All images were acquired with the same microscopy settings, scale bar = 15 µm. Images were analysed with Fiji and average fluorescence intensities per cell were determined.

Coloured points show single cell measurements with colours indicating biological replicate, black circles show averages and error bars indicate standard error of the mean. Statistical analysis was performed with Students t-test where all KOs were tested against the WT. (**B**) Seahorse assay to assess extracellular acidification rates (ECAR) after addition of Oligomycin and Rotenone (Rot)/Antimycin A (AA). Experiment was repeated 3 times and blue lines indicate timing of medium/inhibitor addition. Data is from the same experiment as shown in Fig. 4D. Error bars indicate standard error of the mean. (**C**) Oxygen consumption rates (OCR) and ECAR after the addition of Rotenone A/AA and 2-Deoxy-D-Glucose (2-DG) (data from an independent experiment). Experiment was repeated 3 times and blue lines indicate timing of medium/inhibitor addition. Error bars indicate standard error of the mean. (**D**) Cumulative heat measured by nano-calorimetry over time (left panel). Protein amount in nano-calorimetry samples over time (right panel). N indicates the number of biological replicates. Error bars indicate standard error of the mean. Dashed lines are linear interpolations. (**E**) ATP:ADP ratio in selected KO lines as determined by mass spectrometry. Error bars indicate standard error of the mean. Colored dots represent three biological replicates (B1-B3).
p-Values: *** < 0.0001, ** < 0.001, * < 0.01, ns = < 1.